A COMPARISON OF A SHOCK-CAPTURING TECHNIQUE WITH EXPERIMENTAL DATA FOR

THREE-DIMENSIONAL INTERNAL FLOWS

By Leroy L. Presley

NASA Ames Research Center

SUMMARY

Shock-capturing solutions for an axisymmetric supersonic inlet at small angles of attack have been obtained. Good overall agreement between the shock-capturing solutions and experimental data have been shown except in regions of strong viscous effects or boundary-layer removal. Although the results indicate a strong potential for the use of shock-capturing or finite-difference solutions for internal flows, improvement in the ability to handle the reflection of strong shockwaves having downstream Mach numbers near 1 is needed.

INTRODUCTION

Traditional approaches to the design of axisymmetric supersonic inlets have employed the method of characteristics (refs. 1 to 3). References 2 and 3 include engineering modeling of the viscous effects, with reference 3 incorporating the effects of the boundary layer on the inviscid core flow. For two-dimensional flows — including axisymmetric flows — the method of characteristics provides a standard for any other computational technique. However, extension of the method of characteristics to three-dimensional flows, particularly complex internal flows, presents a very formidable task.

Recent developments in the use of finite-difference techniques show promise for application to three-dimensional internal flows. References 4 and 5 have been concerned with solutions to the flow about shuttle-type vehicles, both with diffuse (captured) and discrete bow shockwaves. References 6 and 7 describe techniques to fit discrete shockwaves into the computational mesh. A comparison of a discrete-shock, finite-difference technique with the method of characteristics for planar internal flows was given in reference 7; agreement between the two techniques was excellent. An advantage in using the finite-difference codes referenced above, as opposed to the method of characteristics, is that embedded shockwaves are captured in the finite-difference mesh without requiring any special logic.

The present paper describes an adaptation of the shock-capturing technique of reference 4 to the particular problem of inviscid flow in axisymmetric supersonic inlets at small angles of attack. (Many helpful suggestions concerning the present paper were made by Paul Kutler.) Comparison of the theoretical solutions with experimental data for the $M_\infty = 3.5$ inlet described in reference 2 is presented. The present shock-capturing solutions represent the

first step in a long range program that will ultimately incorporate discrete shockwaves, boundary-layer effects, mass exchange, and an arbitrary body cross section. The computer code for this analysis was developed by Dennis J. Maine, Computer Science Corporation.

SYMBOLS

a   local speed of sound

k $\dfrac{\gamma - 1}{2\gamma}$

M   Mach number

p   pressure normalized by the free-stream stagnation pressure

q   total velocity normalized by the maximum adiabatic velocity

r   radius from axis of symmetry

u   z-component of velocity

v   r-component of velocity

w ϕ-component of velocity

Z   axial coordinate from centerbody tip

α angle of attack

γ ratio of specific heats

δ boundary surface angle

ρ density

ϕ meridional coordinate

Subscripts:

a   annulus

b   centerbody

c   end of cone

i   index in ξ direction

j   index in ϕ direction

o   outer boundary

t   stagnation conditions

∞   free-stream conditions

Superscripts:

n   array of known flow properties

n+1   advanced array of flow properties

METHOD OF ANALYSIS

General Equations

The technique used in the present analysis is a direct adaptation of the shock-capturing technique presented in references 4 and 5. The major details of the analysis will be presented here, primarily for reasons of completeness. The equations of motion can be written in conservative form, using vector notation and cylindrical coordinates as

$$\tilde{E}_Z + \tilde{F}_r + \tilde{G}_\phi + \tilde{H} = 0 \tag{1}$$

where the $\tilde{E}$, $\tilde{F}$, $\tilde{G}$ and $\tilde{H}$ vector components are defined as:

$$\tilde{E} = \begin{bmatrix} \rho u \\ kp + \rho u^2 \\ \rho uv \\ \rho uw \end{bmatrix} \;\; ; \;\; \tilde{F} = \begin{bmatrix} \rho v \\ \rho uv \\ kp + \rho v^2 \\ \rho vw \end{bmatrix} \;\; ; \;\; \tilde{G} = \frac{1}{r} \begin{bmatrix} \rho w \\ \rho uw \\ \rho vw \\ kp + \rho w^2 \end{bmatrix} \;\; ; \;\; \tilde{H} = \frac{1}{r} \begin{bmatrix} \rho v \\ \rho uv \\ \rho(v^2 - w^2) \\ 2\rho vw \end{bmatrix}$$

Equation (1), which represents the continuity and the three momentum equations, comprises a complete set when coupled with the energy equation in the following form:

$$p = \rho(1 - q^2) \tag{2}$$

where

$$q = \sqrt{u^2 + v^2 + w^2} \tag{3}$$

In applying shock-capturing techniques to the computation of internal flows, it is most convenient to transform the physical coordinate system to one wherein the distance between the inner and outer computational boundaries is normalized. This is done by the following coordinate transformation:

$$Z = Z \;\; ; \;\; \xi = \frac{r - r_b}{r_o - r_b} = \frac{r - r_b}{\omega} \;\; ; \;\; \phi = \phi \tag{4}$$

where, for the case considered here and as shown in figure 1(a), the inner and outer boundaries are given respectively by

$$r_b = r_b(Z) \; ; \; r_o = r_o(Z) \tag{5}$$

It should be noted that, for an axially symmetric configuration, the inner and outer boundaries are independent of the meridional angle.

The conservative form of the equations of motion, equation (1), can be retained in the transformed coordinate system as:

$$E_Z + G_\xi + G_\phi + H = 0 \tag{6}$$

where new variables are defined as follows:

$$\left. \begin{array}{l} E = \tilde{E} \\[4pt] F = \tilde{F} \dfrac{\partial \xi}{\partial r} + \tilde{E} \dfrac{\partial \xi}{\partial Z} \\[8pt] G = \tilde{G} \\[4pt] H = \tilde{H} - \tilde{E} \dfrac{\partial^2 \xi}{\partial Z \, \partial \xi} \end{array} \right\} \tag{7}$$

The transformation derivatives are

$$\frac{\partial \xi}{\partial Z} = \frac{-\dfrac{\partial r_b}{\partial Z} - \xi \left(\dfrac{\partial r_o}{\partial \xi} - \dfrac{\partial r_b}{\partial \xi} \right)}{\omega} \; ; \; \frac{\partial \xi}{\partial r} = \frac{1}{\omega} \; ; \; \frac{\partial^2 \xi}{\partial Z \, \partial \xi} = \frac{-\left(\dfrac{\partial r_o}{\partial \xi} - \dfrac{\partial r_b}{\partial \xi} \right)}{\omega} \tag{8}$$

A plane of known flow quantities at some constant Z^n is required to initiate the solution. Within this plane, an array of discrete points is identified (fig. 1(b)) such that along each meridional ray, there are N_ξ points indexed by $1 \leqslant i \leqslant N_\xi$, and there are N_ϕ meridional rays indexed by $1 \leqslant j \leqslant N_\phi$. A step size consistent with the stability requirements of the differential equations is first determined for advancing the solution to Z^{n+1}. Since only supersonic flows are considered in the present analysis, the Z-axis is the hyperbolic coordinate. For each point in the flow field a minimum of four step sizes, corresponding to the four characteristic directions, must be found as follows:

$$\Delta Z = \frac{\Delta \xi}{\sigma_p}$$

and

$$\Delta Z = \frac{\Delta \phi}{\sigma_q} \tag{9}$$

The maximum eigenvalues are given by

$$\sigma_p = [\sigma(p)]_{\text{local max}} = \max \left(|\sigma_1^M|, |\sigma_2^M| \right) \Bigg\}$$

$$\sigma_q = [\sigma(\alpha)]_{\text{local max}} = \max \left(|\sigma_1^N|, |\sigma_2^N| \right) \Bigg\} \tag{10}$$

where

$$\sigma_{1,2}^M = \frac{\partial \xi}{\partial Z} + \frac{uv \pm a\sqrt{u^2 + v^2 - a^2}}{\omega(u^2 - a^2)}$$

and

$$\sigma_{1,2}^N = \frac{1}{r} \left(\frac{uw \pm a\sqrt{u^2 + w^2 - a^2}}{(u^2 - a^2)} \right) \tag{11}$$

Advancing the solution to Z^{n+1} is controlled by the smallest step size determined for the entire array at Z^n.

New conservative variables, $E_{1,2,3,4}$, are found at step Z^{n+1} using MacCormick's second-order predictor-corrector technique. Some modification to the indexing for these equations is required, depending upon the region of the flow being analyzed, as shown in figure 1(a). These predictor difference equations are given by

(a) For conical, external, and internal flows, where $1 \leqslant i \leqslant N_\xi - 1$ and $1 \leqslant j \leqslant N_\phi$,

$$\overline{E_{ij}^{n+1}} = E_{ij}^n - \frac{\Delta Z}{\Delta \xi}\left(F_{i+1,j}^n - F_{ij}^n\right) - \frac{\Delta Z}{\Delta \phi}\left(G_{i,j+1}^n - G_{ij}^n\right) - \Delta Z H_{ij}^n \tag{12}$$

(b) For conical and external flows, where $i = N_\xi$ and $1 \leqslant j \leqslant N_\phi$, the predicted values are set equal to the free-stream values, which will be defined later.

(c) For internal flows, where $i = N_\xi$ and $1 \leqslant j \leqslant N_\phi$,

$$\overline{E_{N_\xi,j}^{n+1}} = E_{N_\xi,j}^n - \frac{\Delta Z}{\Delta \xi}\left(F_{N_\xi,j}^n - F_{N_\xi-1,j}^n\right) - \frac{\Delta Z}{\Delta \phi}\left(G_{N_\xi,j+1}^n - G_{N_\xi,j}^n\right) - \Delta Z H_{N_\xi,j}^n \tag{13}$$

where the superbar denotes predicted values at Z^{n+1}. The computations are carried out on only one side of the plane of symmetry, $0 \leqslant \phi \leqslant \pi$. For the predictor step, information at $\phi = \pi + \Delta\phi$ is needed, while (as will be seen shortly) information at $\phi = -\Delta\phi$ is needed for the corrector step. This information is obtained by simply mirroring w (i.e., changing the sign of w) across the plane of symmetry at the appropriate points and using the values of p, ρ, u, and v from the mirror image point.

The corrector difference equations are given by

627

(a) For conical and external flows, where $2 \leq i \leq N_\xi$ and $1 \leq j \leq N_\phi$, and for internal flows, where $2 \leq i \leq N_\xi - 1$ and $1 \leq j \leq N_\phi$,

$$E_{i,j}^{n+1} = \frac{1}{2}\left[E_{i,j}^n + \overline{E_{i,j}^{n+1}} - \frac{\Delta Z}{\Delta \xi}\left(\overline{F_{i,j}^{n+1}} - \overline{F_{i-1,j}^{n+1}} \right) - \frac{\Delta Z}{\Delta \phi}\left(\overline{G_{i,j}^{n+1}} - \overline{G_{i,j-1}^{n+1}} \right) - \Delta Z \overline{H_{i,j}^{n+1}} \right]$$

(14)

(b) For conical, external, and internal flows, where $i = 1$ and $1 \leq j \leq N_\phi$,

$$E_{1,j}^{n+1} = \frac{1}{2}\left[E_{1,j}^n + \overline{E_{1,j}^{n+1}} - \frac{\Delta Z}{\Delta \xi}\left(\overline{F_{2,j}^{n+1}} - \overline{F_{1,j}^{n+1}} \right) - \frac{\Delta Z}{\Delta \phi}\left(\overline{G_{1,j}^{n+1}} - \overline{G_{1,j-1}^{n+1}} \right) \right.$$

$$\left. - \Delta Z \overline{H_{1,j}^{n+1}} + \frac{\Delta Z}{\Delta \xi}\left(F_{3,j}^n - 2F_{2,j}^n + F_{1,j}^n \right) \right]$$

(15)

(c) For internal flows, where $i = N_\xi$ and $1 \leq j \leq N_\phi$,

$$E_{N_\xi,j}^{n+1} = \frac{1}{2}\left[E_{N_\xi,j}^n + \overline{E_{N_\xi,j}^{n+1}} - \frac{\Delta Z}{\Delta \xi}\left(\overline{F_{N_\xi,j}^{n+1}} - \overline{F_{N_\xi-1,j}^{n+1}} \right) \right.$$

$$- \frac{\Delta Z}{\Delta \phi}\left(\overline{G_{N_\xi,j}^{n+1}} - \overline{G_{N_\xi,j-1}^{n+1}} \right) - \Delta Z \overline{H_{N_\xi,j}^{n+1}}$$

$$\left. + \frac{\Delta Z}{\Delta \xi}\left(F_{N_\xi,j}^n - 2F_{N_\xi-1,j}^n + F_{N_\xi-2,j}^n \right) \right]$$

(16)

After both the predictor and the corrector steps, the conservative variables $E_{1,2,3,4}$ must be decoded to yield the physical variables $p, \rho, u, v,$ and w such that new predicted or corrected conservative variables $F, G,$ and H can be found. Decoding is accomplished by the following equations:

$$\left. \begin{array}{l} v = \dfrac{E_3}{E_1} \\[2ex] w = \dfrac{E_4}{E_1} \\[2ex] u = \dfrac{E_2 + \sqrt{E_2^2 - 4kE_1^2(1 - k)(1 - v^2 - w^2)}}{2E_1(1 - k)} \\[2ex] \rho = \dfrac{E_1}{u} \\[2ex] p = \rho(1 - u^2 - v^2 - w^2) \end{array} \right\}$$

(17)

After the advanced array is decoded, the flow along the centerbody and annulus boundaries will not necessarily satisfy the tangency requirement. As described in reference 8, the velocity vector at the wall must be rotated through a small angle, Δv, and the wall pressure corrected using the Prandtl-Meyer relationship. The turning angle Δv for all j is found as follows:

(a) For the centerbody,

$$\Delta v = \sin^{-1} \frac{-\hat{u}_1^{n+1} \tan \delta_b^{n+1} + \hat{v}_1^{n+1}}{\hat{q}_1^{n+1} \left(\tan^2 \delta_b^{n+1} + 1\right)^{1/2}} \tag{18}$$

where the carets over the symbols denote the decoded values from the corrector equations (i.e., those values that do not satisfy tangency).

(b) For the annulus,

$$\Delta v = \sin^{-1} \frac{\hat{u}_{N_\xi}^{n+1} \tan \delta_o^{n+1} - \hat{v}_{N_\xi}^{n+1}}{\hat{q}_{N_\xi}^{n+1} \left(\tan^2 \delta_o^{n+1} + 1\right)^{1/2}} \tag{19}$$

The pressure ratio associated with this turning angle is found from

$$\frac{p^{n+1}}{\hat{p}^{n+1}} = 1 - \gamma \mathcal{M}^{n+1} \Delta v + \gamma \left(\frac{\mathcal{M}^{n+1}}{M^{n+1}}\right)\left[\frac{\gamma+1}{4}\left(\mathcal{M}^{n+1}\right)^2 - 1\right]\Delta v^2 \tag{20}$$

where:

$$\mathcal{M} = \frac{M}{\sqrt{M^2 - 1}}$$

and

$$M = \frac{\hat{q}^2}{1 - \frac{1}{5}\hat{q}^2}$$

Note that if $\Delta v > 0$, an expansion will result, while, if $\Delta v < 0$, a compression will result. The new corrected wall pressure, consistent with the tangency condition, is

$$p^{n+1} = \hat{p}^{n+1} \frac{p^{n+1}}{\hat{p}^{n+1}} \tag{21}$$

and the corresponding density is

$$\rho^{n+1} \left(p^{n+1} \right)^{1/\gamma} \tag{22}$$

This relationship for density assumes that the entropy on the centerbody and annulus is everywhere equal to the free-stream values. Once the pressure and density are known, the total velocity is found from

$$q^{n+1} = \sqrt{1 - \left(\frac{p}{\rho} \right)^{n+1}} \tag{23}$$

and the individual velocity components are

$$u^{n+1} = \frac{q^{n+1} \left[\hat{u}^{n+1} + (M/N^2) \tan \delta \right]}{L}$$

$$v^{n+1} = \frac{q^{n+1} (\hat{v}^{n+1} - M/N^2)}{L} \tag{24}$$

$$w^{n+1} = \frac{q^{n+1} \hat{w}^{n+1}}{L}$$

The quantities L, M, and N are

$$L = \left[\left(\hat{u}^{n+1} + \frac{M}{N^2} \tan \delta \right)^2 + \left(\hat{v}^{n+1} - \frac{M}{N^2} \right)^2 + \left(\hat{w}^{n+1} \right)^2 \right]^{1/2}$$

$$M = \hat{u}^{n+1} \tan \delta + \hat{v}^{n+1} \tag{25}$$

$$N = \sqrt{\tan^2 \delta + 1}$$

The angle δ in equations (24) and (25) can be either the surface angle of the centerbody or the annulus at Z^{n+1}.

Method of Solution

Input to the program consists of the free-stream Mach number, the number of points N_ξ and N_ϕ (both of which are held constant throughout the solution), body coordinates (which herein are only a function of Z), and the initial angle of the conical tip. The remaining free-stream input quantities are calculated as follows:

$$P_\infty = \left(1 + \frac{1}{5} M_\infty^2 \right)^{-7/2} \tag{26a}$$

$$\rho_\infty = \left(1 + \frac{1}{5} M_\infty^2 \right)^{-5/2} \tag{26b}$$

$$q_\infty = \left[\frac{M_\infty{}^2}{5}\left(1 + \frac{1}{5}M_\infty{}^2\right)^{1/2}\right]\Bigg\}$$ (26c)

$$n_\infty = q_\infty \cos \alpha$$ (26d)

$$v_\infty = q_\infty \sin \alpha \cos \phi$$ (26e)

$$w_\infty = q_\infty \sin \alpha \sin \phi$$ (26f)

The body coordinates are entered at discrete Z locations. For any three points on either the centerbody or annulus, a quadratic of the form $r = aZ^2 + bZ + c$ was determined. Choice of which coordinates to use for defining the coefficients was determined such that for any Z^{n+1}, determined from $Z^{n+1} = Z^n + \Delta Z$, two of the three points should have $Z > Z^{n+1}$. No explicit attempt at smoothing the angles at the input points was made; however, the present technique has been found to provide a satisfactory representation of the actual contours. The slope of any Z location was found by differentiating the above.

Solution of the conical flow is obtained by an iterative method. First, an outer computational boundary for both the conical and external flowfield must be found that will allow the shockwave from the cone tip to be captured between the centerbody surface and the outer boundary. As shown in figure 1, this boundary is taken to be inclined at an angle, relative to the axis of symmetry of the inlet, that is, equal to the angle of attack plus the planar shockwave angle for a flow deflection equal to the cone half-angle. Similar to the technique of reference 9, the free-stream quantities are assigned between the outer boundary and the cone surface at some initial Z start. The solution is advanced N_ξ steps in Z. Since the flow is conical, these values can be inserted at Z start and the solution again advanced N_ξ steps in Z. This cycling continues until the pressures on the cone at the end of the Nth cycle agree to within an ϵ of 0.0001 of those on the N-1th cycle. The solution was then taken to have converged, and these final flow quantities were assigned to the end of the conical flow zone Z_c. (The location of Z_c is somewhat arbitrary, here taken as $Z_c = 1$ (see fig. 1(a)), but it should always be less than or equal to the portion of the centerbody that can be represented as a cone.) Usually, convergence was obtained within eight cycles for the cases considered here.

After the conical flow was defined, the solution was advanced to the plane of the annulus lip. Here, the mesh is renoded to provide N_ξ points between the centerbody and the annulus lip. For the remainder of the solution, the outer boundary r_0 is the radius of the annulus. If the external flow outer boundary fell outside the annulus lip, the flow properties at the renoded radial points were found using linear interpolation in the external flow solution. If the external flow outer boundary fell inside the annulus lip, linear interpolation was still used, but free-stream flow quantities were assigned between the external flow outer boundary and the annulus lip.

631

Computation of the internal flow continues until the end of the input coordinates. No attempt to define the external flow beyond the plane of the annulus lip was made in this study.

RESULTS AND DISCUSSION

Coordinates of the $M_\infty = 3.5$ axisymmetric supersonic inlet, for which shock-capturing solutions have been obtained herein, are given in table 1, and shown schematically in figure 2. This inlet, which resulted from the design study of reference 2, has the feature that the minimum area remains in nearly the same location, relative to the annulus, as the centerbody is translated forward for off-design ($M_\infty < 3.5$) operation. To obtain maximum performance with this inlet, it is necessary to remove the boundary layer in regions of strong adverse pressure gradients, such as produced by shockwave boundary-layer interactions. Regions of boundary-layer removal remain fixed on the annulus but, through a complicated porting system, move rearward on the centerbody as it is translated forward. (See ref. 2 for details.) Since, in this analysis, boundary-layer effects and mass exchange through the boundaries were not considered, discussion of this boundary-layer removal system is important only insofar as indicating regions wherein good agreement between theoretical calculations and experimental data should not be expected.

Any new computational technique should be compared with a standard solution before being applied to more generalized problems. As shown in reference 7, excellent agreement between a discrete-shock, finite-difference technique and the method of characteristics was obtained for planar internal flows, with good qualitative agreement also being obtained with a straight finite-difference method (shock-capturing technique). It remains to be shown that similar agreement between a shock-capturing solution and the method of characteristics can be obtained for axisymmetric flows, particularly when using a shock-capturing technique developed for three-dimensional flows. A shockwave pattern obtained from the method of characteristics for the inlet at $M_\infty = 3.5$, $\alpha = 0°$, with the centerbody in the design position (herein defined as the position wherein the shockwave from the centerbody tip hits the annulus lip at $M_\infty = 3.5$) is shown in figure 3. Corresponding static pressure distributions on the centerbody and annulus, obtained using the method of characteristics, are shown in figure 4, along with the pressure distributions obtained by using the shock-capturing technique. For all shock-capturing solutions obtained herein, 20 intervals in the ξ direction and 10 intervals in the ϕ direction were used. The shock-capturing solution agrees very well with the method of characteristics up to the second shockwave reflection on the centerbody. This is a fairly strong shockwave reflection, with the method of characteristics indicating a downstream Mach number less than 1.2. Failure of the shock-capturing solution at this point is due to the Mach number becoming subsonic in the interaction region. Overshoots in static pressure, and hence undershoots in Mach number, are typical of the solution of reflecting oblique shockwaves using MacCormack's second-order-accurate differencing in a shock-capturing technique (ref. 10). Several possibilities exist that can possibly resolve this situation: (1) incorporation of higher-order differencing terms, as described in reference 10; (2) incorporation of a damping term near the

shockwaves, as was used in reference 11; (3) incorporation of a technique for allowing the wall entropy to change across reflection regions; or (4) incorporation of discrete shockwaves into the solution. At present, all four of these possibilities are being examined. However, it can be said at this point that until the failure occurs, the solution obtained by the shock-capturing technique agrees well with that obtained by the method of characteristics.

A comparison of the shock-capturing solution discussed above with experimental data is shown in figure 5. Good overall agreement with the experimental data is obtained at $\alpha = 0°$, except in the regions of boundary-layer removal. The experimental data indicate shockwave intersections with the annulus and centerbody slightly ahead of the predictions of the shock-capturing technique. This is reasonable, since the presence of boundary-layer effects in the experimental data would tend to displace the shockwave interactions forward.

An angle of attack solution ($\alpha = 5°$ for the same centerbody location and M_∞ as the above calculations) is shown in figure 6. Again, the solution fails (at station $Z/r_a = 4.5$) due to the Mach number becoming subsonic in the strong interaction region; nevertheless, some qualitative conclusions concerning angle-of-attack effects can be drawn. Static pressures along the windward, $\phi = 0$, and leeward, $\phi = \pi$ meridians for both the annulus and centerbody are shown. Comparison with the solution shown in figure 5 shows that the magnitude of the pressure rise across the shockwave reflections is markedly increased, particularly on the centerbody. Further, evidence that the solution is producing a plausible reproduction of the physical flow is indicated by the behavior of the pressure distribution near the annulus lip on the windward meridian. Here, the shockwave from the centerbody tip should pass inside of the annulus lip and, since the initial angle of the annulus lip is about one degree, a local expansion should be generated at the annulus lip. The decrease of pressure indicated by the solution on the windward meridian near the annulus lip $2.86 \leq Z/r_a \leq 3.1$ is in agreement with the postulated physical flow.

All of the angle-of-attack experimental data that will be discussed herein is for angles of attack of 3°. In the following paragraphs, two different Mach numbers, and hence, two sets of different centerbody location data, will be discussed. The pattern will be first to show an $\alpha = 0°$ solution for the inlet and then an angle of attack solution and corresponding comparison with experimental data. Angle-of-attack effects on the internal flow pattern will thereby be identified.

The first Mach number data that will be discussed is for $M_\infty = 3.3$, where a forward centerbody translation $\Delta Z/r_a = 0.356$ was required. Note that even a small change in angle of attack requires a change in centerbody position for optimum inlet operation. At this M_∞ and $\alpha = 0°$, complete solutions were obtained to $Z/r_a = 5.0$, which is beyond the minimum area of the inlet (fig. 7). The corresponding solution for $\alpha = 3°$ is shown in figure 8. Although the angle-of-attack effects here are not as large as shown in figure 6, there is an indication that the strength of the shock reflections on the leeward side are increased. Here again, a complete solution was not obtained because the Mach number became subsonic in the strong reflection region near $Z/r_a = 4.8$ on the centerbody. Most of the experimental data are for the leeward side, with good qualitative agreement being obtained (except for the viscous effects

633

noted earlier). Some data on the windward side of the annulus were obtained and these show the same qualitative behavior with respect to the leeward data as indicated by the shock-capturing solutions.

The last Mach number data that will be discussed is for $M_\infty = 2.5$, where a forward translation $\Delta Z/r_a = 0.855$ was required. The $\alpha = 0°$ solution is shown in figure 9, where a complete solution beyond the minimum area was obtained. At this Mach number, a complete solution was also obtained at angle of attack, and again the strength of the shockwave reflections was increased (fig. 10). For this case, the centerbody was extended sufficiently far forward that some expansion to pressures lower than the conical values was expected, and this is shown by both the data and the shock-capturing solution. Again invoking the qualifications on the agreement due to viscous effects, good qualitative agreement between the shock-capturing solution and experimental data was obtained.

CONCLUDING REMARKS

For all of the internal flows examined herein, several observations can be made:

(1) A solution given by the shock-capturing technique agrees well with one given by the method of characteristics for $\alpha = 0°$.

(2) Second-order-accurate differencing can fail in regions near the reflection of strong shockwaves where the downstream Mach number is near 1. Several possibilities such as higher-order differencing, damping terms near the shockwaves, wall entropy correction, and discrete shockwaves are being investigated to determine if this failure can be overcome.

(3) Shock-capturing solutions agree well with experimental data, except in regions of strong viscous effects and boundary-layer removal.

REFERENCES

1. Sorenson, V. L.: Computer Program for Calculating Flow Fields in Supersonic Inlets. NASA TN D-2897, 1965.

2. Syberg, J., and Hickcox, T. E.: Design of a Bleed System for a Mach 3.5 Inlet. NASA CR-2187, 1974.

3. Maslowe, S. A., and Benson, J. L.: Computer Program for the Design and Analysis of Hypersonic Inlets. NASA CR-77749, 1964.

4. Kutler, P., Lomax, H., and Warming, R. F.: Computation of Space Shuttle Flow Fields Using Noncentered Finite-Difference Schemes. AIAA Paper 72-193, 1972.

5. Kutler, P., Reinhardt, W. A., and Warming, R. F.: Numerical Calculations of Multishocked Three-Dimensional Supersonic Flow Fields with Real Gas Effects. AIAA Journal, vol. 11, May 1973, pp. 651-664.

6. Moretti, G.: Complicated One-Dimensional Flows. Polytechnic Institute of Brooklyn, PIBAL Report No. 71-25, September 1971.

7. Presley, L. L., and Kutler, P.: Comparison of a Discrete-Shock Finite-Difference Technique and the Method of Characteristics for Calculating Internal Supersonic Flows. NASA paper presented at AIAA Computational Fluid Dynamics Conference (Palm Springs, Calif.), July 19-24, 1973.

8. Abbett, M. J.: Boundary Condition Calculation Procedures for Inviscid Supersonic Flow Fields. Proceedings, AIAA Computational Fluid Dynamics Conference (Palm Springs, Calif.), July 19-24, 1973, pp. 153-172.

9. Kutler, P., and Lomax, H.: Shock-Capturing, Finite-Difference Approach to Supersonic Flows. J. Spacecraft and Rockets, vol. 8, no. 12, pp. 1175-1182.

10. Anderson, D. A.: A Comparison of Numerical Solutions to the Inviscid Equations of Fluid Motion. Journal of Computational Physics, vol. 15, no. 1, pp. 1-20.

11. Kutler, P., Sakel, L., and Aiello, G.: On the Shock-on-Shock Interaction Problem. AIAA Paper 74-524, 1974.

TABLE 1.- $M_\infty = 3.5$ INLET CONTOUR DEFINITION

Z/r_a	r/r_a	Z/r_a	r/r_a
Centerbody		Annulus	
0.0	0.0	2.86	1.0
4.0	0.70532	3.1	1.004188
4.1	0.7228	3.2	1.0054
4.2	0.7387	3.4	1.0051
4.3	0.7512	3.6	0.99996
4.4	0.759	3.8	0.9882
4.5	0.7625	4.0	0.9681
4.55	0.763	4.1	0.954
4.6	0.7625	4.2	0.9364
4.65	0.7611	4.25	0.9261
4.7	0.7585	4.3	0.9154
4.8	0.7504	4.4	0.8949
4.9	0.7391	4.5	0.8768
5.1	0.7120	4.55	0.8695
5.3	0.6829	4.6	0.864
5.5	0.6525	4.65	0.86
5.6	0.6362	4.7	0.8572
5.7	0.618	4.8	0.8533
5.8	0.5973	4.9	0.8511
5.9	0.5744	5.0	0.8502
6.0	0.5467	5.1	0.85
		5.6	0.85
		5.8	0.8574
		5.9	0.8646
		6.0	0.8735
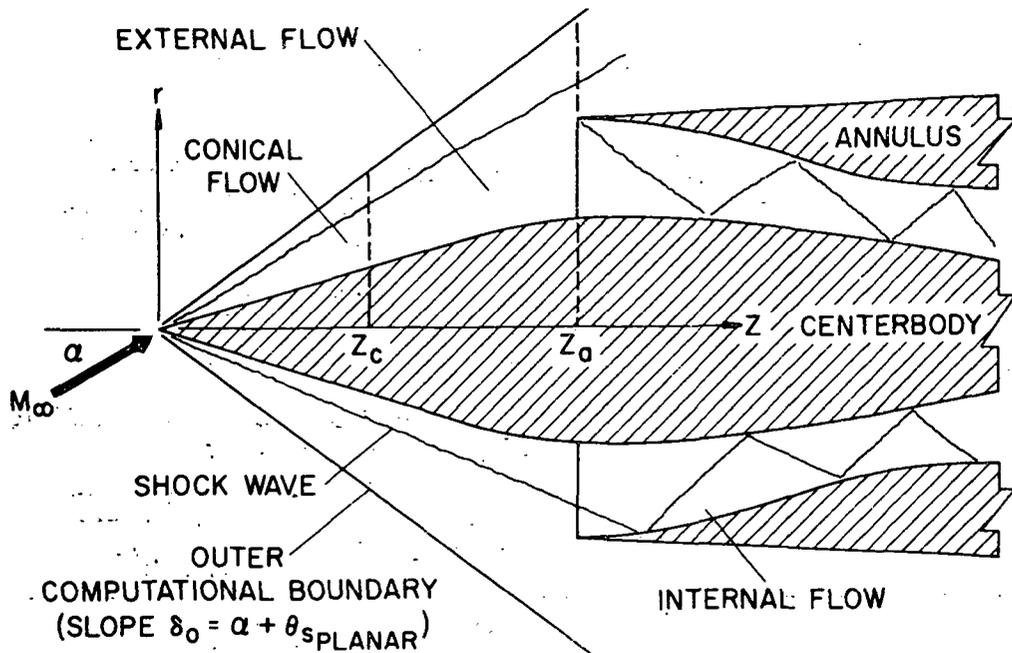
(a).— Schematic diagram of computational domains.
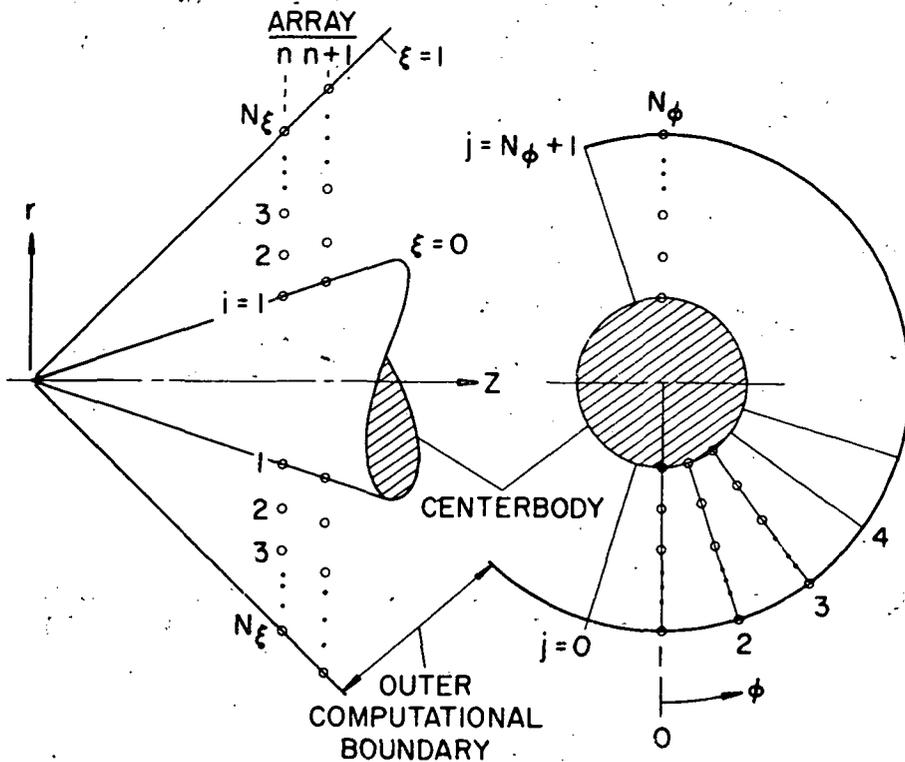
(b).— Diagram of indexing scheme for shock-capturing technique.

Figure 1.— Details of flow-field model.
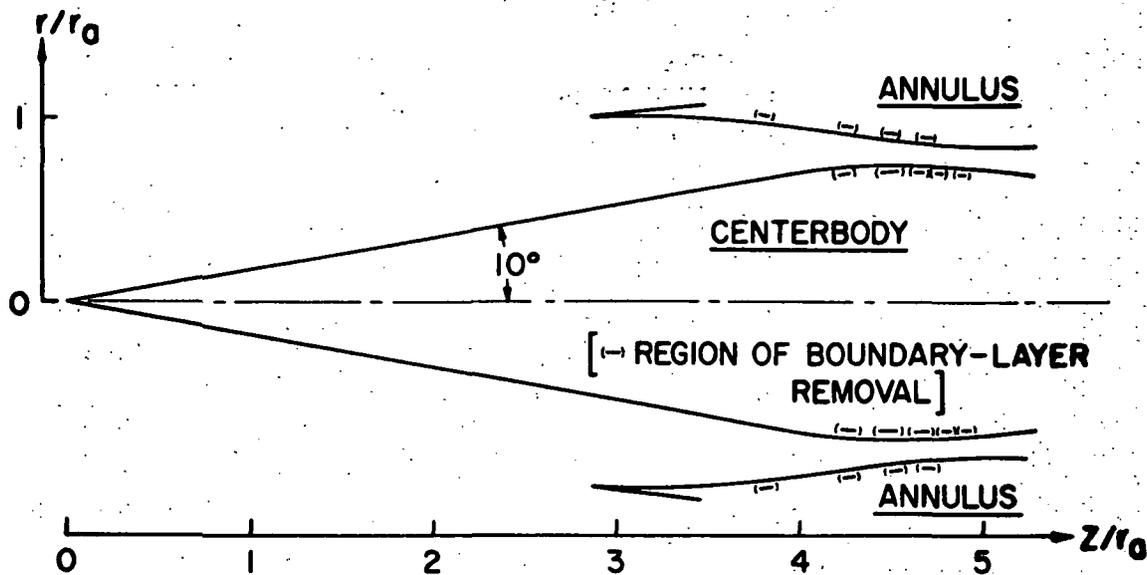
Figure 2.— Contours of M_∞ = 3.5 inlet.
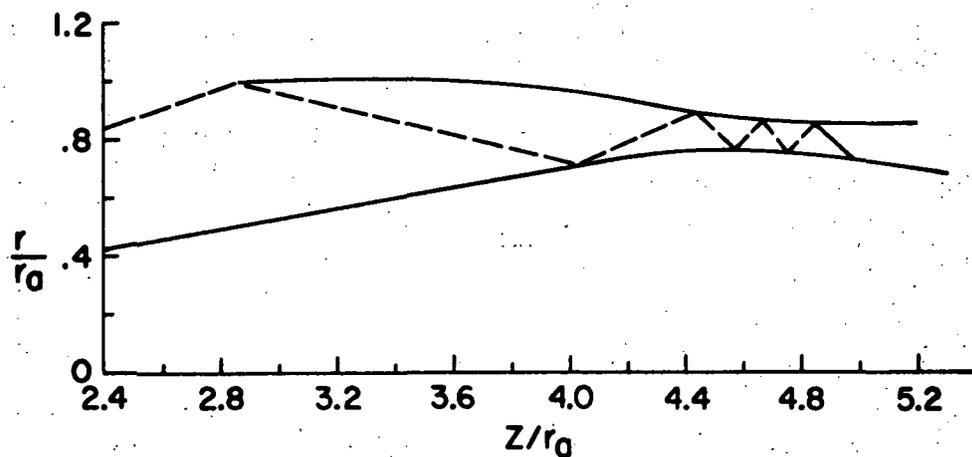
Figure 3.— Shock wave pattern given by the method of characteristics for M_∞ = 3.5, α = 0°, and design centerbody location, $\Delta Z/r_a$ = 0.

Figure 4.— Comparison of pressure distributions given by the shock-capturing technique and the method of characteristics for $M_\infty = 3.5$, $\alpha = 0°$, and design centerbody location, $\Delta Z/r_a = 0$.
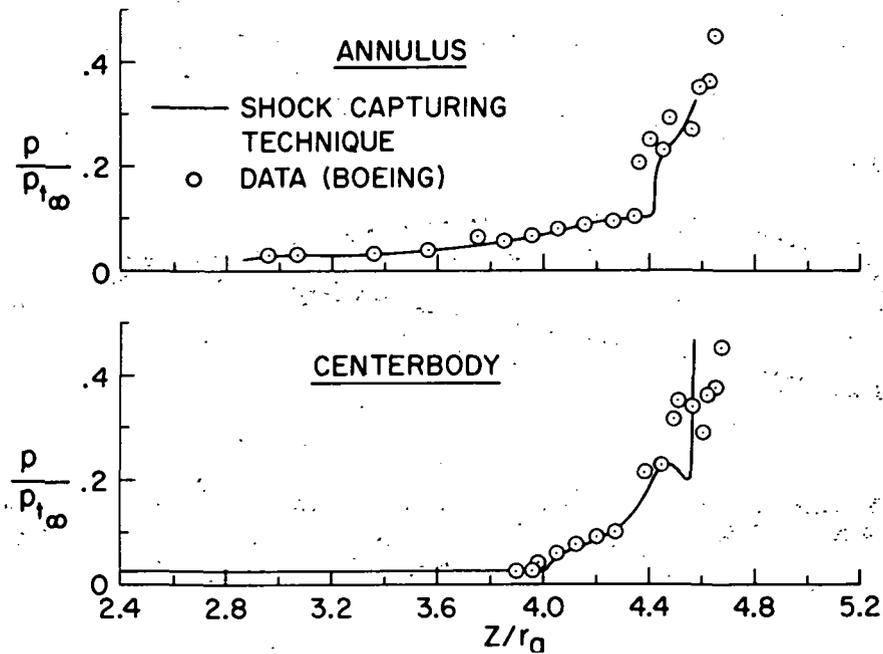
Figure 5.— Comparison of pressure distribution given by the shock-capturing technique with experimental for $M_\infty = 3.5$, $\alpha = 0°$, and design centerbody location, $\Delta Z/r_a = 0$.
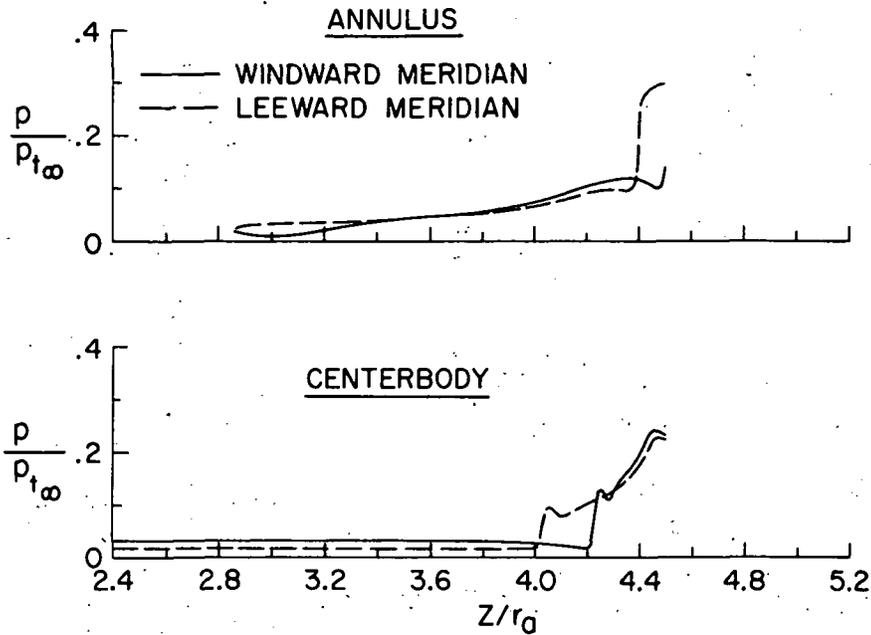
Figure 6.— Shock-capturing solution for $M_\infty = 3.5$, $\alpha = 5°$, and design centerbody position, $\Delta Z/r_a = 0$.
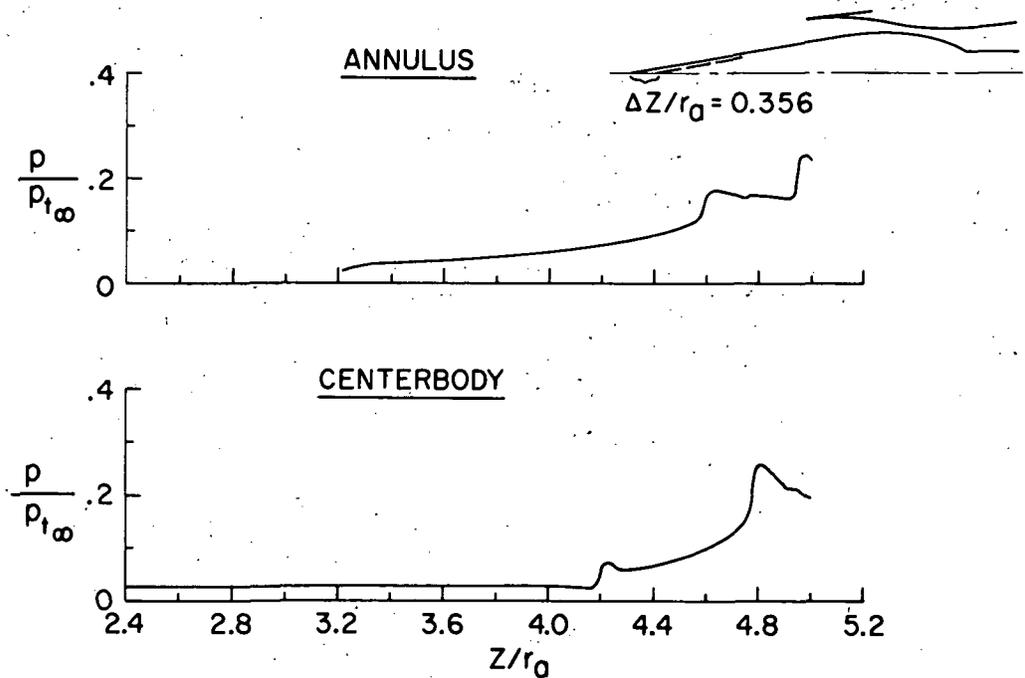
Figure 7.— Shock-capturing solution for $M_\infty = 3.3$, $\alpha = 0°$, and $\Delta Z/r_a = 0.356$.
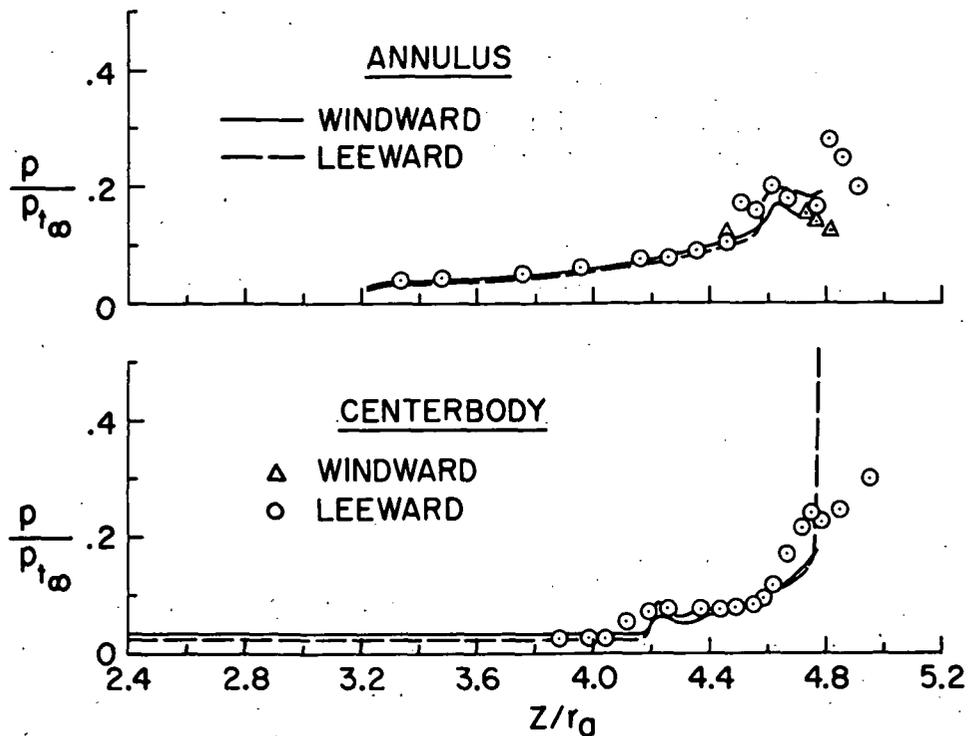
Figure 8.— Comparison of pressure distributions given by shock-capturing technique with experimental data for $M_\infty = 3.3$, $\alpha = 3°$, and $\Delta Z/r_a = 0.356$.
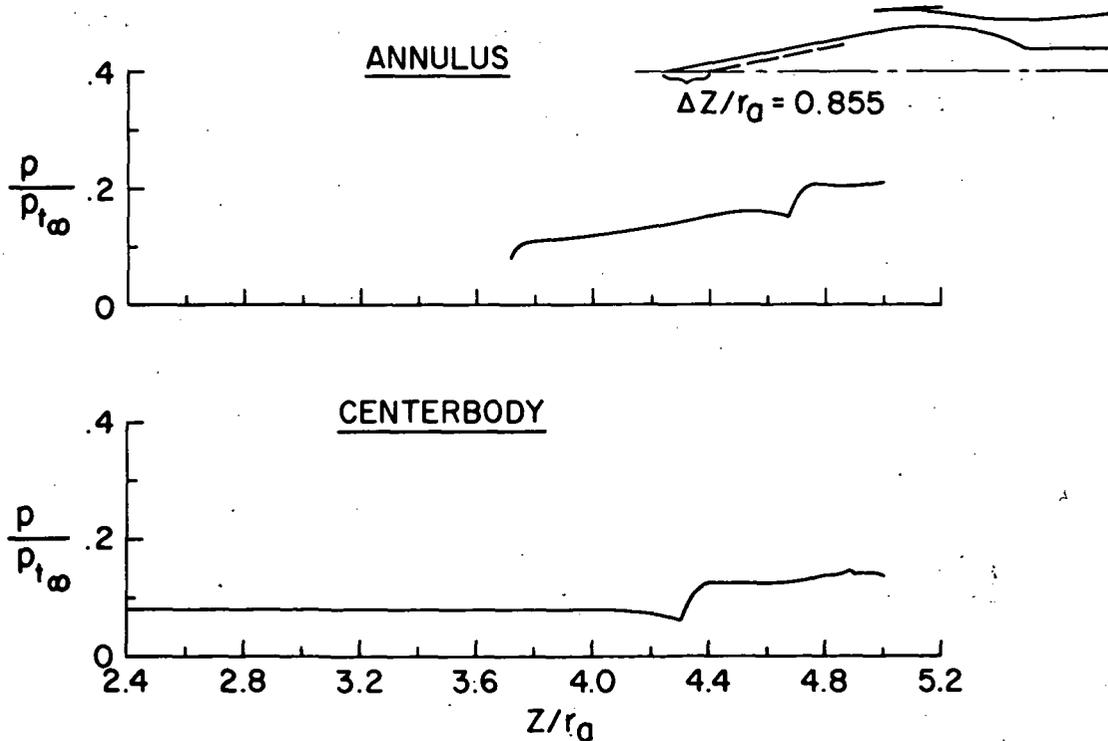

Figure 9.— Shock-capturing solution for $M_\infty = 2.5$, $\alpha = 0°$, and $\Delta Z/r_a = 0.855$.
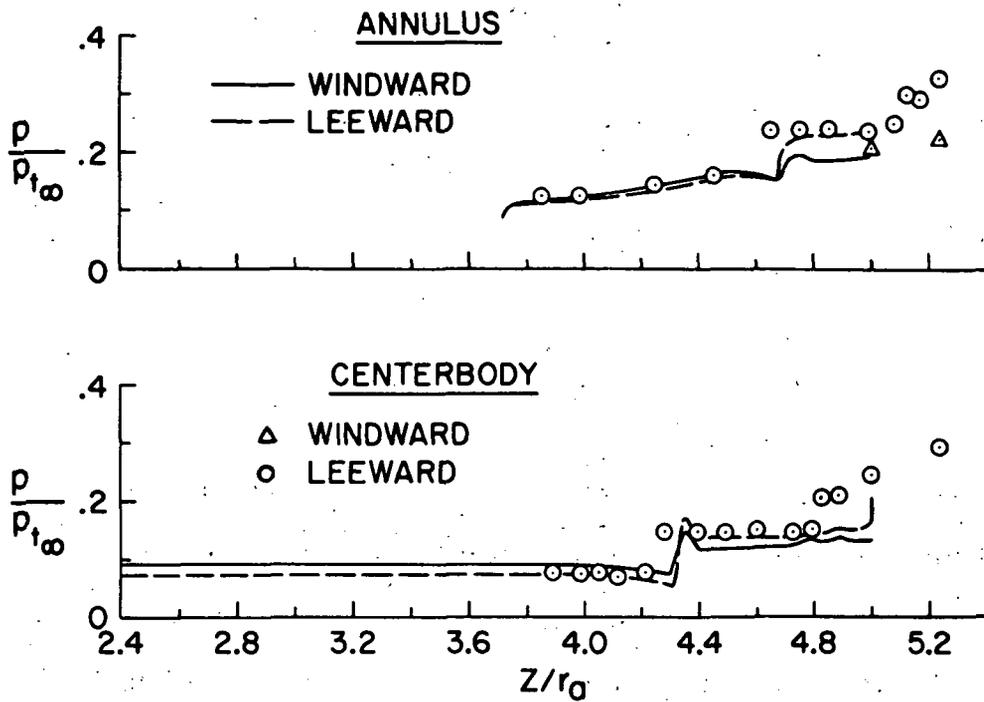
Figure 10.— Comparison of pressure distributions given by shock-capturing technique with experimental data for $M_\infty = 2.5$, $\alpha = 3°$, and $\Delta Z/r_a = 0.855$.